Versatile compact atomic source for high-resolution dual atom interferometry

T. Müller, T. Wendrich, M. Gilowski, C. Jentsch, E. M. Rasel, and W. Ertmer
Institut für Quantenoptik, Leibniz Universität Hannover, Welfengarten 1, D-30167 Hannover, Germany
(Received 30 May 2007; published 13 December 2007)

We present a compact ^{87}Rb atomic source for high precision dual atom interferometers. The source is based on a double-stage magneto-optical trap (MOT) design, consisting of a two-dimensional (2D) -MOT for efficient loading of a 3D-MOT. The accumulated atoms are precisely launched in a horizontal moving molasses. Our source generates a high atomic flux ($>10^{10}$ atoms/s) with precise and flexibly tunable atomic trajectories as required for high resolution Sagnac atom interferometry. We characterize the performance of the source with respect to the relevant parameters of the launched atoms, i.e., temperature, absolute velocity, and pointing, by utilizing time-of-flight techniques and velocity selective Raman transitions.

DOI: 10.1103/PhysRevA.76.063611 PACS number(s): 03.75.Dg, 39.20.+q, 32.80.Pj, 39.10.+j

I. INTRODUCTION

In the recent past atom interferometry has become a promising technique for high resolution measurements particularly in fundamental physics and for multidisciplinary purposes. Examples are the measurement of the photon recoil for the determination of the fine-structure constant [1], the measurement of the gravitational constant G [2], as well as gravimeters [3] and gravity gradiometers [4] or atomic gyroscopes [5]. All these experiments benefit from a variety of well-developed techniques to coherently manipulate, cool, and trap atoms with laser light [6].

One of the experimental key elements of atom interferometry is the source of atomic matter waves. In this paper we present the design and study of a compact highly stable atomic source for a transportable atomic Sagnac sensor, i.e., a dual Raman-type atom interferometer based on the Mach-Zehnder geometry [7], see Figs. 1 and 2. We discuss the performance of the source with respect to the requirements imposed by an atomic Sagnac interferometer using free-falling atoms as an ideal inertial reference. From the measured noise properties of the atomic source we estimate the contributions to the sensitivity for rotations of our future gyroscope. Our design is based on a two stage magneto-optical trap (MOT) [8]: A two-dimensional trap [9] creates an atomic beam for efficient loading of a following three-dimensional (3D) -MOT. The trapped atoms are subsequently launched in a moving molasses (see, for example, Ref. [10]) to imprint a precise velocity onto the atoms. This design combines the advantages of the previous source concepts for atomic gyroscopes, which have used thermal beams [5] or a 3D-MOT loaded from a background vapor [11], i.e., a high atomic flux combined with a well-defined atomic velocity. Our source is especially compact compared to other state-of-the-art source concepts like Zeeman slowers [12] or thermal beam devices.

This paper is organized as follows: In Sec. II we discuss the requirements for a source imposed by Sagnac atom interferometers, which guided us to our source design. The experimental setup of the atomic source is described in Sec. III. In Secs. IV and V, we characterize the performance of our realized source with respect to the atomic flux and the launch parameters of the atomic ensemble. Finally, a conclusion and outlook for the precision measurements of rotations with this device is given in Sec. VI.

II. SOURCE REQUIREMENTS FOR ATOMIC SAGNAC INTERFEROMETER

For atom or light interferometers the achievable sensitivity is determined by a scaling factor, i.e., the resulting phase shift induced by the effect to be measured, divided by the minimal resolvable phase shift of the interferometer. The scaling factor for rotation measurements in atom interferometers can be calculated analogous to the optical Sagnac interferometer. The phase, induced by a rotation $\vec{\Omega}$ of the laboratory system with respect to the interferometer, is proportional to the scalar product of $\vec{\Omega}$ with the area $\vec{A}$ enclosed by the interferometer and to the atomic mass m divided by Planks constant h [13]:

$$\Delta\varphi_{rot} = \frac{4\pi m\vec{A}\cdot\vec{\Omega}}{h}. \tag{1}$$

This relation shows that atomic Sagnac interferometers measure a projection of the enclosed area $\vec{A}$ with respect to the rotation $\vec{\Omega}$. Therefore the area $\vec{A}$ has to be stable both in absolute value as well as in its orientation to the rotation vector to guarantee a well-defined scaling factor. For the case of the Raman-type Mach-Zehnder atom interferometer using free-falling atoms (see Fig. 2 and [2–5,7,11]) that we focus on in this paper, the enclosed area is spanned by the atomic drift velocity $\vec{v}_{at}$ and the effective velocity $\vec{v}_{bs}=\hbar\vec{k}_{bs}/m$ transferred by the atom-light interaction during the coherent

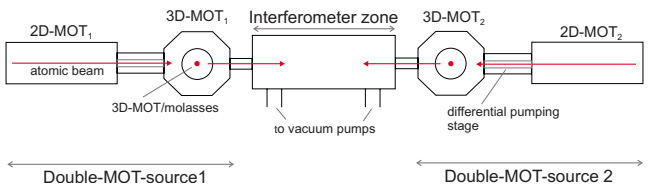

FIG. 1. (Color online) Schematic of the experimental apparatus for the atomic inertial sensor, top view. The interferometer is shown in Fig. 2 in more detail.

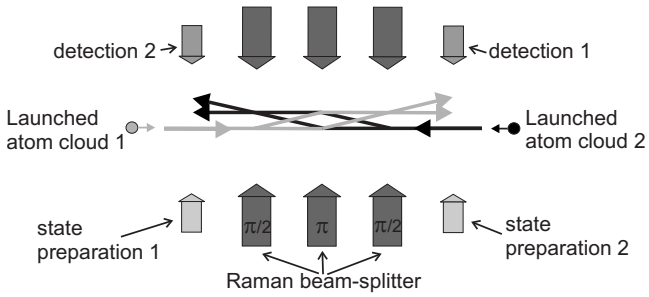

FIG. 2. Diagram of the prospective dual Mach-Zehnder interferometer for precision inertial sensing, top view. The atoms are launched from two sides in the interferometer and each cloud is prepared in the suitable input state before interacting with the Raman beam-splitters. A pulse sequence consisting of consecutive $\pi/2$-π-$\pi/2$-pulses representing a beam-splitting, a mirror, and a second beam-splitting pulse, respectively, realizes a Mach-Zehnder-like interferometer geometry. The phase difference between the two interferometer arms is determined by detecting the intensity of the two output ports.

beam-splitting, redirecting and recombination of the matter waves,

$$A = L^2 \frac{v_{bs}}{v_{at}} \sin \vartheta. \tag{2}$$

L denotes the spatial separation between the atom-light interaction zones and ϑ the angle between the atomic drift velocity and the beam-splitting laser used for the coherent manipulation of the atoms. It is notable that the atomic mass drops out of the scaling factor for a given momentum $\hbar\vec{k}_{bs}$. Apart from the Sagnac effect, the interferometer is also sensitive to accelerations $\vec{a}$ along the direction of the Raman laser beams. Therefore an accelerational phase shift is induced, given by $\Delta\varphi_{acc}=\vec{a}\vec{k}_{bs}T^2$, where T is the time of free evolution of the atomic ensemble in-between the atom-light interactions.

From these relations, a set of requirements can be derived for the design of a compact Sagnac interferometer and for the atomic sources employed in the device. First of all, high stability and precise control of the absolute atomic velocity and pointing of the atomic source are required since the atomic velocity enters the scaling factor and determines the orientation of the interferometers sensitive axis in combination with the orientation of the beam splitting lasers.

Moreover, the atomic Sagnac sensor must discriminate between rotations and accelerations. According to Eqs. (1) and (2) a distinction is possible by using a differential measurement based on two simultaneous atom interferometers with reversed atomic beams [5]. This results in a change of the sign of the Sagnac phase, and hence a subtraction or addition of the two interferometers' signals gives access to a purely rotational or accelerational induced phase shift, respectively. In order to apply this method, both sources should emit counterpropagating ensembles of atoms with equal and stable features such as velocity and pointing.

In addition, the ratio of the scaling factors for accelerations and rotations can be modified by changing the atomic velocity $\vec{v}_{at}$. On the one hand, higher atomic velocities and a larger length L of the setup allow one to keep a constant enclosed area A while at the same time providing a lower sensitivity for accelerations and inertial noise. As an example, in our interferometer with $L=75$ mm and $|\vec{v}_{at}|=3$ m/s the phase shift induced by the earth rotation rate is equal to a phase shift induced by accelerations of 9×10^{-4} m/s^2. Concerning an imperfect suppression of accelerations, this indicates the necessity of isolating the interferometer from the laboratory vibrational noise when aiming for resolutions of fractions of the earth rotation, i.e., 10^{-8} rad/s or better. On the other hand, a compact device with restricted dimensions L on the order of a few centimeters necessitates the use of cold and slow atoms increasing the ratio of v_{bs}/v_{at} [see Eq. (2)] and thus enlarging the enclosed area A. An atomic velocity of 1–20 m/s therefore represents a good choice, allowing for a rotational resolution of 10^{-8} rad/s with a reasonable resolution of the phase shift in the interferometer of about 1 mrad.

Another important aspect of the source is the temperature of the atomic ensemble. For inertial measurements the Raman beam-splitters are strongly velocity selective [3,5,11]. As a result, the efficiency of the beam-splitting is reduced for finite temperature. This reduces the effective interferometer signal and leads to an incoherent background. These effects decrease the sensitivity of the interferometer.

Finally, a high flux of the source, comparable to thermal atomic beams, helps to achieve a good signal-to-noise ratio and enhances the ultimately achievable phase resolution of the interferometer, given by the atomic shot-noise limit. Additionally, a high atomic flux allows for short preparation times of the atomic samples with respect to the measurement time. This increases the cycling rate of the measurement, minimizing the noise contribution by the Dick effect [14,15]. In this respect, the best noise characteristic would be achieved by performing a continuous measurement [16].

III. DESCRIPTION OF THE ATOMIC SOURCE AND EXPERIMENTAL SETUP

We have developed a compact atomic source, which consists of a so-called double-MOT-system, for an atomic Sagnac sensor. In our apparatus a 3D-MOT is loaded by a cold and slow atomic beam emitted from a 2D-MOT. The source design with a 2D-MOT followed by a 3D-MOT allows the combination of a high atomic flux and precisely controlled atomic velocities as required for precision rotation measurements, see Sec. II, in an optimal way. The alternative of a source consisting of a single 2D-MOT would be suitable concerning the needed atomic flux, but does not provide the needed precision in velocity control. Additionally, a perfect overlap of the trajectories of atoms emitted horizontally by two sources for dual interferometry is hardly possible due to the gravitational acceleration. However, a single 3D-MOT is well-suited to provide high accuracies in the atomic velocities and trajectories. Therefore, after release out of the 3D-MOT, the atoms are launched by a moving molasses toward the interferometer. Thus the atomic velocity can be controlled with high accuracy by adjusting the frequency differ-

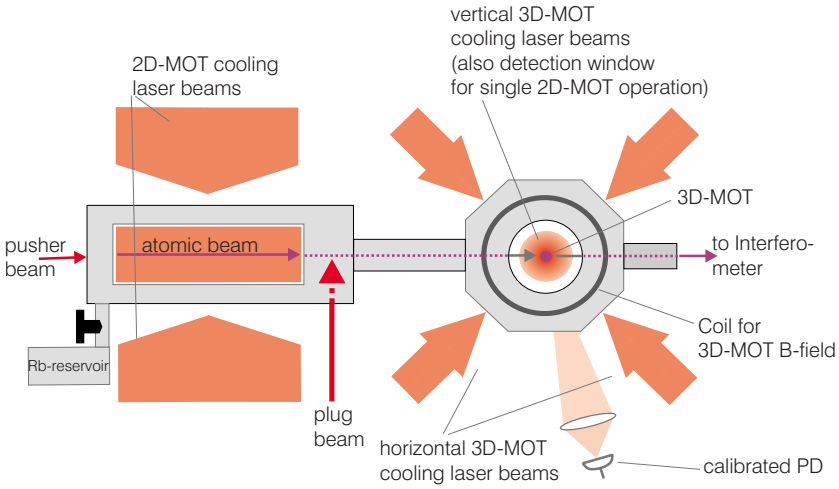

FIG. 3. (Color online) Schematic of one double-MOT atomic source (top view). Not shown are the coils for 2D-MOT magnetic field generation.

ence between the molasses laser beams [17]; but it is hardly possible with a single 3D-MOT loaded from background vapor to achieve an atomic flux comparable to the one generated with a 2D-MOT. This limitation could only be overcome when using high laser power and high atomic vapor pressure. Since the second measure would lead to a significantly increased collision rate during the free-falling flight the useful atomic flux for the interferometry provided by the single 3D-MOT does not reach the 2D-MOT atomic flux. The use of other high-flux alternatives based on thermal sources, such as Zeeman slowers, as a presource rather than the 2D-MOT has been excluded due to our self-restraint of a compact apparatus.

Our realization of the moving molasses permits individual control of the horizontal and the vertical atomic velocity component. In this way, we can vary the horizontal velocity between 2.5 and 5 m/s and, at the same time, compensate for gravity by adjusting the vertical velocity between 0 and 1 m/s, resulting in flat parabolic atomic trajectories. This possibility of velocity variation allows more flexible time dependent systematic studies or even the reduction of the impact of time-dependent noise sources. The chosen trajectories and velocity values are a compromise between accelerational noise sensitivity and compactness of the sensor.

An additional advantage of our double-MOT-system is that the use of a 2D-MOT as the first source stage in principle also allows one to operate the atom interferometer continuously and benefit from the advantage of this scheme [16]. In this case, the 3D stage is operated without the magnetic field and used only for molasses cooling and redirecting the atoms. For these further manipulations, the use of a 2D-MOT is well-suited, as it is forming a brilliant and already slow atomic beam, with similar atomic velocities as produced by the moving molasses.

In principle, the choice of the flat parabolic trajectories allows the measurement of all components of the rotation vector $\vec{\Omega}$, as it permits one to apply the Raman-beam-splitters from several perpendicular directions and in novel interferometer topologies as demonstrated in Ref. [18]. However, our design is optimized for measurements of the rotation component Ω_z, parallel to gravity.

A schematic of the source unit is shown in Fig. 3. One double-MOT consists of two separate chambers that are connected via a differential pumping stage. In the first chamber the 2D-MOT is loaded from rubidium background vapor and the second chamber at a pressure of about 10^{-8} mbar houses the 3D-MOT. The vacuum system is mainly based on custom-made parts to keep the apparatus as compact as possible. The overall volume of one source unit including fiber couplers, beam shaping optics, and magnetic coils is about $35\times30\times25$ cm^3. The nonmagnetic chambers are made of aluminum, providing large optical access. The optical substrates are directly sealed to the individual chambers, either using vacuum compatible glue (for the 2D-MOT), or indium-sealings (for the 3D-MOT). The Rb background pressure in the 2D-MOT is maintained by a heatable vacuum tube containing a Rb ampule which is connected to the 2D-MOT via a valve. The 2D-MOT and the 3D-MOT chambers have a rectangular and an eight-cornered shape, respectively (see Fig. 3). The rectangular shape of the 2D-MOT chamber reflects the transverse cooling volume of 80×18 mm^2, similar to [19]. The 3D-stage is connected to the interferometer via a vacuum adapter with a rectangular aperture of size 30×10 mm^2, which can be displaced vertically to allow for even greater variations of the atomic trajectories from almost flat to steep parabolas with a maximum starting angle of about 18°. The geometry of the 3D-MOT cooling beams is chosen such that the horizontal laser beams are placed at an angle of 45° to the 2D-MOT atomic beam axis, whereas the vertical laser beams are perpendicular to it. The magnetic field for the 3D-MOT is generated with external coils, directly wound onto the chamber, whereas the coils for the 2D-MOT are mounted on a frame rigidly fixed to the chamber.

Two atomic sources of this kind are integrated into our experiment for operating a dual atom interferometer. This setup, shown in Fig. 1, is placed on a single optical breadboard (1.2×0.9 m^2), surrounded by a μ-metal magnetic shield, which suppresses stray magnetic fields by a factor of about 40.

The laser beams for the cooling light are generated by two commercial high power diode laser systems in master oscillator power amplifier (MOPA) configuration (Toptica TA100), delivering 700 mW for the 2D-MOT and 500 mW for the 3D-MOT. From the 3D-MOT laser four independent

laser frequencies are derived for the moving molasses by using acousto-optic modulators (AOMs) in double-pass configuration. This frequency difference can be referenced to a high quality radio-frequency oscillator in order to achieve a higher precision and stability for the atomic velocities. Additionally, this laser generates a light beam copropagating with the cold atomic beam formed by the 2D-MOT, which enhances the forward directed atomic flux thanks to light pressure. This so-called "pusher"-beam (see Fig. 3) is also frequency controlled using a AOM. A self-made external cavity diode laser (ECDL) produces repumping light for atoms in the lower hyperfine level $|F=1\rangle$.

All lasers are frequency controlled using saturated absorption spectroscopy near the D_2 line of ^{87}Rb at 780 nm. The laser sources are placed on a separate optical breadboard and the beams are delivered to the main apparatus with polarization maintaining (PM) optical fibers. In all MOT stages the repumping light is superimposed on the cooling light and delivered to the experiment with the same optical fibers, using one individual fiber for each light beam.

The beam shaping optics at the fiber exits, for example, beam collimation or polarization retarders, are rigidly fixed to the vacuum chamber. Thus the stability of the optical setup is improved with respect to free-space optical paths. Beam diameters are 80×18 mm^2 for the 2D-MOT, and 30 mm for the 3D-MOT.

IV. SINGLE 2D-MOT AND COMBINED DOUBLE-MOT CHARACTERIZATION

A. 2D-MOT characterization

In our source concept, the 2D-MOT replaces a Zeeman slower and generates a large flux of atoms with velocities low enough to be captured by the 3D-MOT or further cooled in the 3D-molasses. The characterization of the 2D-MOT therefore focused on the optimization of the atomic flux and the velocity distribution of the 2D-MOT's atomic beam by tuning the relevant parameters such as laser power, detuning, and the magnetic field gradient ΔB.

The flux and velocity distribution were measured by detecting the atomic fluorescence with a calibrated photodiode while the atoms interact with a retroreflected detection laser beam tuned to the $|F=2\rangle \rightarrow |F'=3\rangle$ transition of the D_2 line. The detection laser beam with a diameter of 5 mm and 0.5 mW power was placed 133 mm downstream from the 2D-MOT exit. For the velocity measurement the atomic beam was chopped with a second transverse, running wave laser beam tuned onto the $|F=2\rangle \rightarrow |F'=3\rangle$ transition deflecting the atoms with its light pressure, the so-called "plug"-beam. Analyzing the time-dependent atom number and integrating over all velocities we can deduce the atomic flux as well as the velocity distribution.

The results for a combined measurement are shown in Fig. 4 for different values of the total cooling laser power and magnetic field gradient. The laser detuning δ for this measurement was $\delta=-1.2\Gamma$ (Γ is the linewidth of the D_2 transition), which was shown to be optimal in a separate measurement. The optimal magnetic field gradient ΔB for a laser power of 200 mW is about 12 G/cm. The measurement

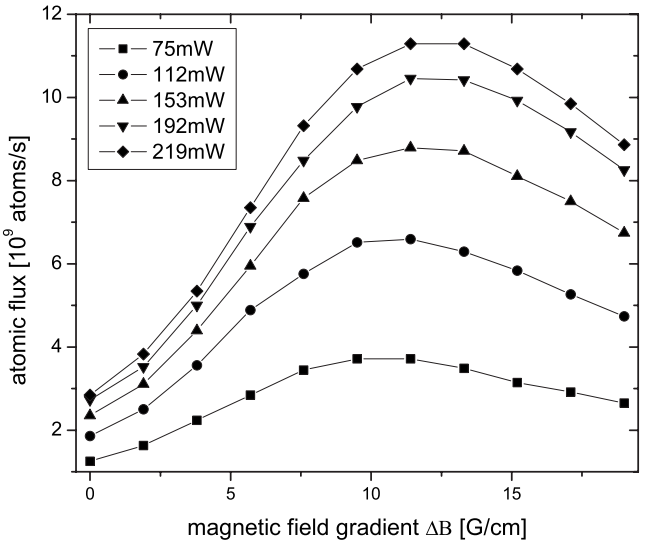

FIG. 4. 2D-MOT atomic flux versus magnetic field gradient for different total cooling laser power. Other experimental parameters are detuning $\delta=-1.2\Gamma$ and Rb-reservoir temperature 120 °C.

shows that the flux can be enhanced by increasing the laser power and saturates at a value of about 200 mW total laser power. The optimal flux achieved in this measurement was 1.1×10^{10} atoms/s. The corresponding velocity distributions (Fig. 5) show that the most probable velocity is less than 20 m/s for all laser powers that have been used in the measurement. Additionally, it shows that increasing the laser power results in higher mean atomic velocities. This is theoretically predicted by a 2D-MOT model, for example derived in Ref. [19].

Previous work by other groups (for example, [9]) showed that additional molasses cooling on the atomic beam axis can also increase the atomic flux and reduce the mean longitudinal velocity. Due to limited optical access on the atomic beam axis we apply a related, but more simple scheme with only one single traveling beam. Without the additional laser beam the velocity distribution on the longitudinal axis of the

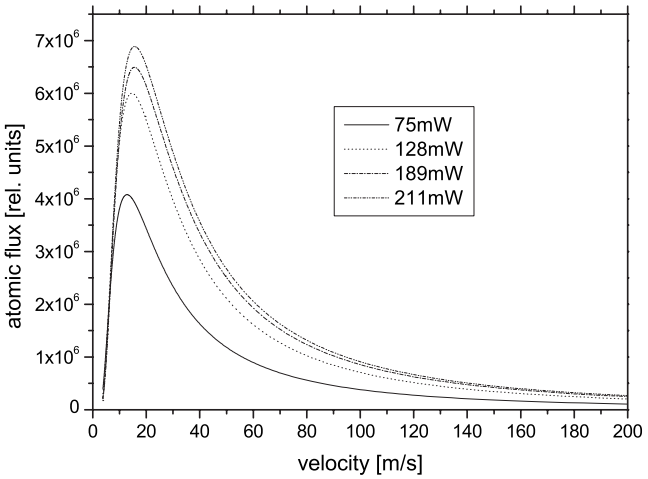

FIG. 5. Velocity distribution of the atomic beam from the 2D-MOT for different total laser power. Recorded with $\delta=-1.2\Gamma$, $\Delta B=12$ G/cm, and 120 °C Rb-reservoir temperature.

atomic beam produced by the pure 2D-MOT is symmetric. The cold atoms move in the direction of the 3D-MOT as well as in the opposing direction, where they are lost. Due to the light pressure induced by the additional laser beam the velocity distribution on the longitudinal axis is shifted, giving a net mean velocity in the direction of the 3D-MOT. For a detuning $\delta=+1.8\Gamma$ to the $|F=2\rangle \rightarrow |F'=3\rangle$ transition and with 0.5 mW power this "pusher" beam enhances the atomic flux by a factor of 4. Since the beam acts on the longitudinal axis, the mean velocity is also slightly increased.

To estimate the beam divergence, we proceeded as follows: By reducing the size of the "plug" beam with a knife edge transversally, a part of the atomic beam is not deflected and can still reach the detection zone. Monitoring the residual detected fluorescence, we can assign a Gaussian profile to the atomic beam. Comparing the measured atomic beam waists at different distances from the 2D-MOT exit, we calculate the divergence to be about 30 mrad.

The performance of the 2D-MOT comes close to that of thermal sources used for atomic Sagnac interferometry [5], while it allows at the same time to keep the setup compact and transportable.

B. 2D-/3D-MOT characterization

In our present interferometer the 2D-MOT serves to quickly load the 3D-MOT. Therefore a major characterization aspect for the combined 2D-/3D-MOT operation was the 3D-MOT loading rate. This loading rate was examined for different parameters (such as the rubidium background pressure in the 2D-MOT) and configurations, with and without the "pushing" laser beam. We infer the loading rate from the time dependent filling of the 3D-MOT, which is deduced from the atomic fluorescence, by switching the 2D-MOT atomic beam. The switching is performed by mechanical shuttering the light and by tuning the magnetic field of the 2D-MOT. Without the 2D-MOT operating, the influx of atoms into the 3D-MOT is completely stopped and we find no detectable filling of the 3D-MOT by residual background Rb atoms. In the realized setup presented in this paper, the saturation of the absolute 3D-MOT atom number is determined by collisions with background (non-Rb) gas atoms with a time constant of about 0.5 s.

We find the following optimal parameters for our 3D-MOT to maximize the loading rate: Detuning $\delta=-3.5\Gamma$ and magnetic field gradient $\Delta B=14.5$ G/cm. Varying the 3D-MOT laser power, we infer a similar dependence like that given in Fig. 4 for the 2D-MOT. Under usual conditions when serving two complete source units we work with 10 mW laser power per 3D-MOT beam, which is at the beginning of saturation.

The dependence of the loading rate on rubidium vapor pressure is displayed in Fig. 6. The Rb pressure is adjusted by tuning the Rb-reservoir temperature. The loading rate does not saturate for the chosen temperatures which still leaves room for a further improvement (compare, for example, [9] for a saturation behavior with increasing Rb-vapor pressure).

The 3D-MOT loading rate can also be enhanced by the use of the "pusher" beam, see Sec. IV A. For the combined

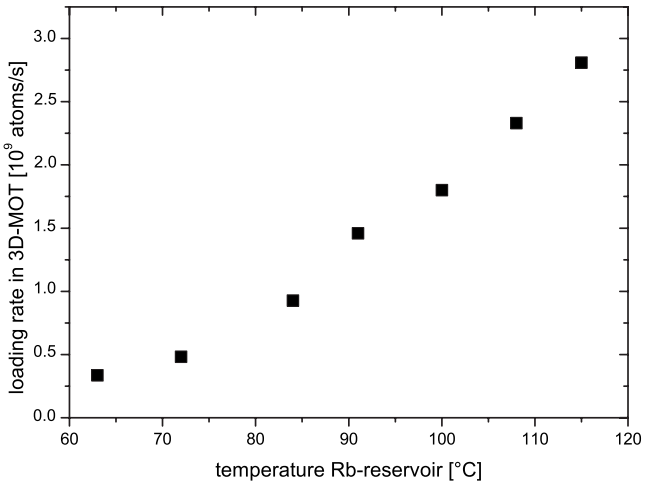

FIG. 6. Influence of the rubidium vapor pressure on the atomic flux measured via the 3D-MOT loading rate. The temperature of the rubidium reservoir relates directly to the pressure. All experimental parameters are given in the text (Sec. IV B).

operation of the 2D-/3D-MOT this laser beam has to be aligned with a slight tilt of about 3° with respect to the atomic beam, to avoid a disturbance of the 3D-MOT. In this configuration, the loading rate can be enhanced by a factor of 3.5 with 0.9 mW light power in the "pusher" beam.

Due to the limited laser power, the simultaneous operation of both atomic sources is performed with lower light power. In addition, we use a moderate rubidium vapor pressure to extend the lifetime of the source. With the resulting parameters such as a total laser power in the 2D-MOT of 130 mW, a total laser power in the 3D-MOT of 60 mW, and a Rb-reservoir temperature of 90 °C we obtain a 3D-MOT loading rate of 5.6×10^9 atoms/s in combination with the additional "pusher" beam, as shown in Fig. 7. With these parameters, the maximum 3D-MOT atom number we obtain is 2×10^9 atoms, which saturates due to collisions with background (non Rb) atoms. Operating the source with all impor-

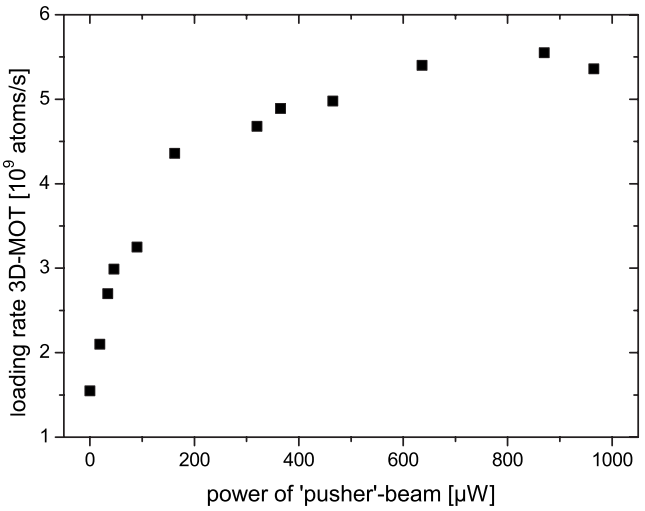

FIG. 7. 3D-MOT loading rate depending on the power of the additional "pusher" beam for the 2D-MOT. An enhancement of the flux and the loading rate at the same time is possible.

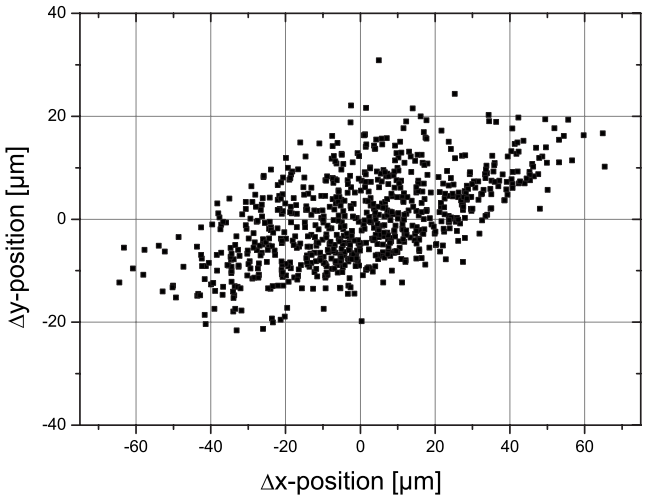

FIG. 8. Position of the atomic cloud in the MOT just before launching. The position is displayed for each dimension relative to the mean value.

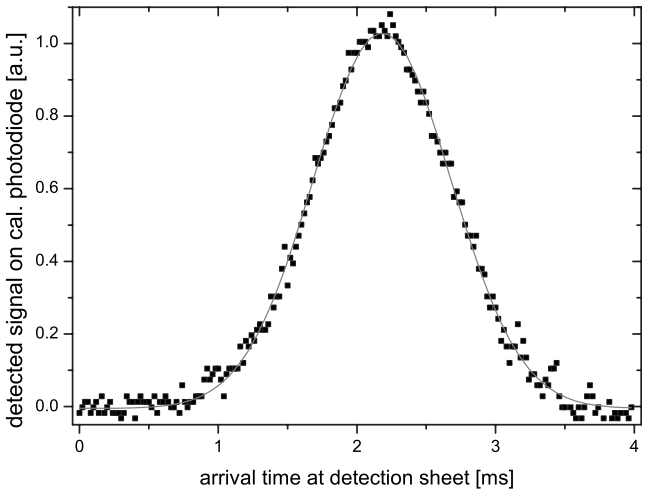

FIG. 9. The atomic velocity and temperature are measured in the interferometer zone in a time-of-flight measurement. The arrival time at a thin sheet of light is recorded and can be converted to a spatial distribution because of the known atomic mean velocity.

tant parameters deeper in the saturated regime, e.g., laser power or Rb vapor pressure, we can obtain loading rates $>10^{10}$ atoms/s.

V. ATOMIC LAUNCH ANALYSIS

In this section, we investigate the features of the emitted atomic ensemble relevant for the determination of the scaling factor such as the accuracy of the forward velocity and pointing and orientation of the source, as well as the parameters determining the effective signal of the interferometer, i.e., the atomic temperature.

To characterize the stability of the starting conditions for the moving molasses, we record the spatial position of the atoms just before the launch. *In situ* images of the fluorescence of the atoms trapped in the MOT are imaged onto a charge-coupled device camera over 30 min while cycling the experiment about 800 times. The result is displayed in Fig. 8. The recorded camera images provide information about the clouds position along the atomic beam propagation axis ("x" dimension) as well as in the direction along the interferometers Raman beam-splitter propagation ("y" dimension). We find standard deviations of $\sigma_x=23$ μm and $\sigma_y=8.5$ μm for the variations of the spatial position. To convert the measured position variations into an uncertainty for the resolution of rotations of the interferometer, the aberrations of the interferometer beam-splitters have to be taken into account [20]. Considering the aberrations given in Ref. [20], we can estimate the position variations to induce an uncertainty in the rotation measurement on the order of less than a few nrad/s, assuming our projected enclosed area A of 22 mm^2.

In the next step of the launch analysis we examine the stability of the starting velocity $\vec{v}_{at}$, beginning with a measurement of the variations of the absolute value $|\vec{v}_{at}|$ with a time-of-flight method. The arrival times of the atomic wave packets were measured at various positions downstream in the interferometer chamber. Each detection zone consists of a thin (0.5 mm) sheet of retroreflected σ^+-polarized light, resonant with the $|F=2\rangle \rightarrow |F'=3\rangle$ transition of the D_2 line. The time dependent fluorescence signal resulting when launching the atoms through the detection zones is recorded by a calibrated photodiode at each zone. A typical measurement curve is shown in Fig. 9. We measure the spatial distance between the detection zones and calculate the absolute velocity $|\vec{v}_{at}|$. This measurement setup is not sensitive to the direction of $\vec{v}_{at}$ (for small misalignments from the perfect direction), since the detection light is perpendicular to the ideal horizontal trajectory. Within the uncertainty of the distance measurement, we find no significant difference between the theoretically calculated and the measured velocity. To analyze the stability, consecutive velocity measurements are performed during a 50 min interval while cycling the experiment. Each measurement point consists of the mean velocity value of 5 min averaging. The result is displayed in Fig. 10: The relative standard deviation of the velocity $\sigma_{|v_{at}|}$ is 3×10^{-4} (which is also the uncertainty of the velocity measurement), with the biggest variation being 1.1×10^{-3}. Additionally, the measured absolute velocity value $|\vec{v}_{at}|$ is the same for both sources to a relative uncertainty of $<3\times10^{-4}$. Assuming the projected enclosed area of our prospective interferometer of 22 mm^2 the measured variations of the absolute velocity would lead to a rotation uncertainty of 5×10^{-9} rad/s. At the same time, the variations of the absolute velocity will lead to changes in the spatial position of the atomic cloud of about 50 μm at the beam splitter position. Analogous to the variation of the clouds starting position, we estimate this effect to induce a rotation uncertainty of a few nrad/s.

The same experimental setup is also used to determine the temperature of the atomic cloud: Thanks to the precisely measured mean velocity, we can convert the time-dependent photodiode signal into a spatial dependence and deduce the diameter of the atomic cloud at different times after the launch. We neglect the finite size of the light sheet (which is small compared to the $e^{-1/2}$ cloud size of 4.5 mm) and assume an isotropic distribution. From this time-of-flight (TOF) experiment we conclude the atomic temperature with

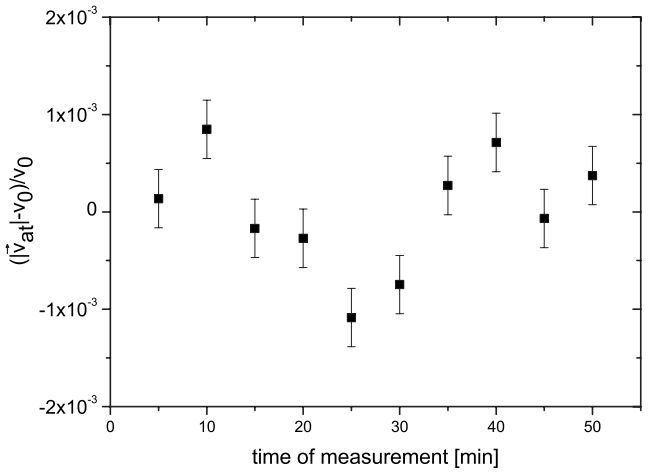

FIG. 10. Relative stability of the measured atomic velocity for cycling time of 50 min. The actual velocity $|\vec{v}_{at}|$ is compared relative to the value v_0, which is calculated from the applied frequency difference for the moving molasses. Each displayed point is the mean value of consecutive measurements, see text for details.

optimized launching parameters to be 8 μK. To minimize the atomic temperature we release the atoms adiabatically [17] at the end of the launch sequence. The launch sequence of the atoms begins with a 1 ms long acceleration phase after switching of the magnetic fields and waiting long enough for the induced eddy currents to vanish. In this acceleration phase the differential detuning for the moving molasses is applied, the overall detuning of the cooling laser is suddenly switched to -1.5Γ, and the laser power is kept constant. For the minimum observed temperature, we suddenly switch afterwards the overall detuning to -12Γ (while keeping the differential detuning) and ramp down the laser power adiabatically in 0.8 ms. The laser beams are switched off completely at the end of this sequence, which releases the atoms, while the cloud of atoms still has been completely inside the diameter of the laser beams, which avoids beam steering problems due to spatial shut-off.

The atomic temperature is also determined in a second complementary measurement by deducing the temperature dependent efficiency of Doppler-sensitive two-photon Raman-transitions. Following the launch, we apply an internal atomic state preparation into the $|F=1,m_F=0\rangle$ state before performing the Raman transitions. We induce the velocity selective Raman transitions between the $|F=1,m_F=0\rangle$ and the $|F=2,m_F=0\rangle$ substates of the $5\,^2S_{1/2}$ level, the so-called "clock-transition" at about 6.834 GHz. To drive the Raman transition, we use two phase-stable, perfectly overlapped laser fields of frequency ω_1 and ω_2, with a frequency difference of about 6.8 GHz. To be Doppler sensitive, both beams interact with the atoms from two directions, see Fig. 11. The laser polarizations are chosen such that only counterpropagating beam pairs can induce a Raman transition. The laser beams, precisely leveled perpendicular to gravity, cross the atomic trajectories nearly perpendicular, but with a small angle deviation θ (with $\vartheta=90°-\theta$), allowing a selection of one of the two driving pairs due to the Doppler effect. The normalized excitation spectrum is obtained by detecting both internal states consecutively. The interaction of the two

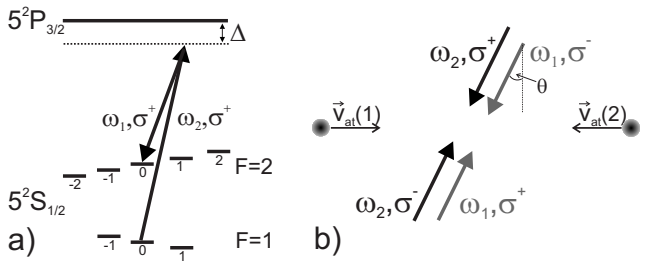

FIG. 11. Schematic of the experimental setup for velocity sensitive Raman transitions. (a) Diagram of the atomic levels included in the Raman transition. Whereas the $5\,^2P_{3/2}$ level is displayed simplified as a single level, the $5\,^2S_{1/2}$ hyperfine manifold is displayed in detail, including the Zeeman-splitting of the different m_F components induced by a magnetic offset field. (b) Diagram of the optical setup for the Raman laser beams, top view. The two atomic ensembles launched with $\vec{v}_{at}(1,2)$ interact from two directions with each of the two Raman laser beams with frequency $\omega_{1,2}$. A transition is only possible with equal polarization in the two Raman laser beams ($\sigma^+-\sigma^+$ or $\sigma^--\sigma^-$) which is used to suppress Doppler insensitive transitions thanks to the chosen polarization configuration. Each of the two atomic ensembles can undergo a resonant transition either for negative or positive detuning relative to the unperturbed atomic transition with one of the resonant beam pairs due to the Doppler effect.

counterpropagating wave packets and the two Raman-beam pairs results in a double resonance as shown in Fig. 12. To determine the maximal obtainable transition probability, we perform Rabi oscillations between the two atomic states by tuning the Raman lasers on one of the two resonances and varying the pulse length, see Fig. 13. We obtain a maximal transition amplitude of 0.33. This result is compared to a theoretical simulation of the temperature-dependent reduction of the transition probability including the dependence to the experimental parameters (like the driving field Rabi frequency). The reduction of the transition amplitude due to

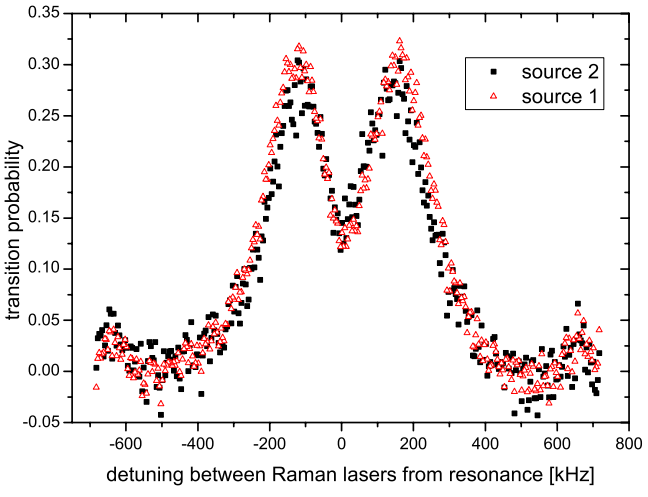

FIG. 12. (Color online) Variation of the frequency difference between the Raman lasers for a velocity selective pulse, compared to the unshifted "clock" transition. The pulse length of about 10 μs was chosen to give maximal transition amplitude for optimal detuning.

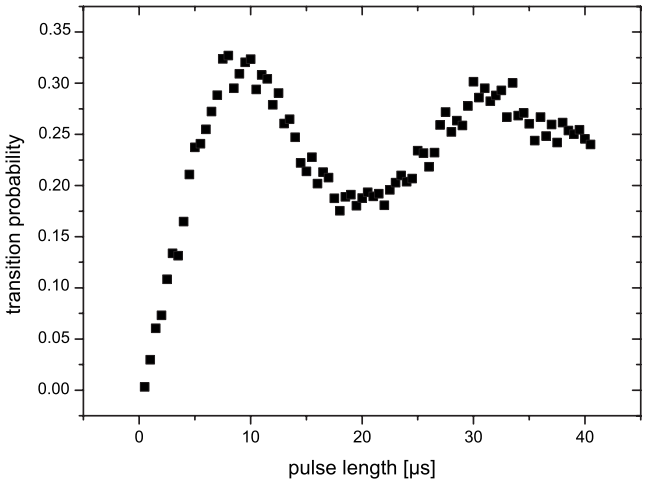

FIG. 13. Variation of the pulse length of a velocity selective Raman transition for optimal detuning (inferred from Fig. 12). The maximal transition probability is related to the atomic temperature, which can be determined by this measurement, in this case 10 μK.

other effects than the temperature is excluded with an independent Doppler-insensitive measurement. Thus we find a temperature of 10 μK, slightly higher than in the TOF measurement. We attribute the internal state preparation before the Raman transitions, which includes optical pumping, to inducing a small additional heating, explaining the difference between the two independent measurements.

The positions of the frequency dependent maxima of the Raman transition shown in Fig. 12 provide additional information about the overlap of the atomic trajectories of both source units. In addition to the detuning of about 130 kHz, which results from the intentionally applied angle $\theta \simeq 12$ mrad, the maxima for the two sources are displaced by about 15 kHz, which corresponds to an angle difference of the atomic trajectories in the horizontal plane of about 1.34 mrad. We can assign the frequency difference of both maxima to a pure angle displacement, because both absolute horizontal velocities $|\vec{v}_{at}|$ have been measured to be equal to much better precision. For the determined angle deviation, we mainly make an undesired, independently determined tilt of the experimental platform during the measurement responsible. Due to the tilt of about 5.2 mrad (with respect to the horizon) the small, ideally vertical atomic velocity component we apply to realize parabolic atomic trajectories is partly converted into a horizontal velocity component. The tilt of the platform will be better controlled for future experiments, either due to passive stability or an active servo loop. Thus subtracting the tilt effect, the two clouds trajectories are parallel to <0.2 mrad, with the residual angle deviation resulting from molasses laser beam misalignment. Converting the atomic velocity direction misalignment into changes in the area A (for the Sagnac measurement) results in a relative variation of only 10^{-6} for A assuming $\vartheta \approx 90°$, changing the measured rotation rate in our interferometer by much less than nrad/s.

The pointing misalignment in the vertical direction was not measured independently, but we estimate the misalignment in the vertical direction to be of the same order as in the horizontal direction, assuming the same accuracy of alignment for all molasses laser beams. The position variation of the atomic cloud at the Raman beam-splitters induced by this estimated horizontal misalignment is about 40 μm, corresponding to a rotation error of few nrad/s, again following the results from Ref. [11].

VI. CONCLUSION AND OUTLOOK

In this paper we have presented a compact atomic source comprising a 2D-MOT- and a 3D-MOT-moving molasses providing precise and stable launch conditions as required for atomic Sagnac interferometers. The flux of the 2D-MOT is comparable to thermal sources and the 3D-MOT loading flux saturates above 10^{10} atoms/s. Under usual operating conditions we load the 3D-MOT with 10^9 atoms in 200 ms. With our measured state preparation efficiency of 70% and the measured efficiency of the Doppler-sensitive Raman transitions of 33% we will be able to operate the interferometer at a cycling rate of 3 Hz with 3×10^8 atoms/s contributing to the measurement signal. Thus the flux of the atomic source will not limit the targeted signal-to-noise ratio of 10^3 or better, which is the current state of the art for cold atom interferometers.

Aiming for resolutions of rotations of better than 10^{-8} rad/s, the performed measurements show that the performance of the realized atomic source will not be a limitation for the short-term sensitivity of the interferometer. We estimate the noise contribution when combining the different noise sources characterized in Sec. V to result in an uncertainty of rotations of roughly 5×10^{-9} rad/s for 1 s measurement time. Assuming these noise sources as dominant, our future Sagnac interferometer can be compared to other state-of-the-art sensors. Thus we find that our sensor will almost rival the most sensitive 3 m long, stationary atomic gyroscope with a sensitivity of 6×10^{-10} rad/s for 1 s integration time which uses thermal beams [5]. The most sensitive gyroscope based on cold atoms has reached a sensitivity for rotations of 2.2×10^{-6} rad/s in 1 s integration time [18], whereas the apparatus is even more compact than ours.

We identified in this paper the velocity stability and the pointing as the most important noise contributions of the atomic source to the performance of our future atomic gyroscope. They can be reduced by improving technical aspects such as the power stability or the optics for beam guiding of the molasses lasers. These measures should additionally allow a further reduction of the atomic temperature. Moreover, our source design permits the planned extension of the velocity control for the two sources, allowing a tuning of both relevant velocity components for each source individually, which leads to a further optimization of the overlap of the atomic trajectories.

Besides the described application for interferometry, the presented source could also be adapted for other kinds of atom optic experiments, where a brilliant atomic source with flexible and precisely controlled atomic velocity in the range of several m/s is desired, for example, the injection of atoms into a guiding potential [21].

Thanks to the compactness of our apparatus we will be able to realize the final atomic sensor as a transportable device. This will be an interesting option for combined measurements with other high resolution atomic or optical sensors [22], allowing the implementation in applied sciences like geology or geodesy such as the search for variations of the Earth's rotation.

ACKNOWLEDGMENTS

We thank J. J. Arlt for a careful reading of the manuscript. This work was supported as part of the SFB 407 of the "Deutsche Forschungsgemeinschaft," as part of the FINAQS cooperation of the European union, as well as part of Project No. 4477 of the ESA.

[1] A. Wicht, J. M. Hensley, E. Sarajlic, and S. Chu, Phys. Scr. **T102**, 82 (2002).
[2] M. Fattori, G. Lamporesi, T. Petelski, J. Stuhler, and G. M. Tino, Phys. Lett. A **318**, 184 (2003).
[3] A. Peters, K. Y. Chung, and S. Chu, Metrologia **38**, 25 (2001).
[4] J. M. McGuirk, G. T. Foster, J. B. Fixler, M. J. Snadden, and M. A. Kasevich, Phys. Rev. A **65**, 033608 (2002).
[5] T. L. Gustavson, A. Landragin, and M. A. Kasevich, Class. Quantum Grav. **17**, 2385 (2000).
[6] H. J. Metcalf and P. van der Straten, *Laser Cooling and Trapping* (Springer, New York, 1999).
[7] C. Jentsch, T. Müller, E. M. Rasel, and W. Ertmer, Gen. Relativ. Gravit. **36**, 2197 (2004).
[8] E. L. Raab, M. Prentiss, A. Cable, S. Chu, and D. E. Pritchard, Phys. Rev. Lett. **59**, 2631 (1987).
[9] K. Dieckmann, R. J. C. Spreeuw, M. Weidemüller, and J. T. M. Walraven, Phys. Rev. A **58**, 3891 (1998).
[10] S. Bize, Y. Sortais, M. S. Santos, C. Mandache, A. Clairon, and C. Salomon, Europhys. Lett. **45**, 558 (1999).
[11] F. Yver-Leduc, P. Cheinet, J. Fils, A. Clairon, N. Dimarcq, D. Holleville, P. Bouyer, and A. Landragin, J. Opt. B: Quantum Semiclassical Opt. **5**, S136 (2003).
[12] C. Slowe, L. Vernac, and L. V. Hau, Rev. Sci. Instrum. **76**, 103101 (2005).
[13] M. Sagnac, Compt. Rend. **157**, 1410 (1913).
[14] G. Santarelli, C. Audoin, A. Makdissi, P. Laurent, G. J. Dick, and A. Clairon, IEEE Trans. Ultrason. Ferroelectr. Freq. Control **45**, 887 (1998).
[15] G. J. Dick, *Proceedings of the 19th Annual Precise Time and Time Interval (PTTI) Applications and Planning Meeting*, Redondo Beach, CA, 1987 (U.S. Naval Observatory, Washington, D.C., 1988), p. 133.
[16] P. Thomann, M. Plimmer, G. Di Domenico, N. Castagna, J. Guéna, G. Dudle, and F. Füzesi, Appl. Phys. B: Lasers Opt. **84**, 659 (2006).
[17] C. Salomon, J. Dalibard, W. D. Phillips, A. Clairon, and S. Guellati, in *Proceedings of the 12th International Conference on Atomic Physics*, Ann Arbor, 1990, edited by R. Lewis and J. C. Zorn, AIP Conf. Proc. No. 233 (AIP, New York, 1991), p. 73.
[18] B. Canuel, F. Leduc, D. Holleville, A. Gauguet, J. Fils, A. Virdis, A. Clairon, N. Dimarcq, Ch. J. Bordé, A. Landragin, and P. Bouyer, Phys. Rev. Lett. **97**, 010402 (2006).
[19] J. Schoser, A. Batär, R. Löw, V. Schweikhard, A. Grabowski, Yu. B. Ovchinnikov, and T. Pfau, Phys. Rev. A **66**, 023410 (2002).
[20] J. Fils, F. Leduc, P. Bouyer, D. Holleville, N. Dimarcq, A. Clairon, and A. Landragin, Eur. Phys. J. D **36**, 257 (2005).
[21] T. Lahaye, J. M. Vogels, K. J. Günter, Z. Wang, J. Dalibard, and D. Guéry-Odelin, Phys. Rev. Lett. **93**, 093003 (2004).
[22] R. W. Dunn, D. E. Shabalin, R. J. Thirkettle, G. J. MacDonald, G. E. Stedman, and K. U. Schreiber, Appl. Opt. **41**, 1685 (2002).